Electronic Supplementary Information

Reticulated carbon nanofiber-encapsulated SnO_2 hollow spheres as high performance anode material for lithium-ion batteries

Ya Chen [a], Lingling Wang [a], Bozhi Yang [a], Jiapeng Lu [a], Minghao Fang [a], Wei Wang [b], Bin Ma [c], Xin Min [a, *]

[a] Engineering Research Center of Ministry of Education for Geological Carbon Storage and Low Carbon Utilization of Resources, Beijing Key Laboratory of Materials Utilization of Nonmetallic Minerals and Solid Wastes, National Laboratory of Mineral Materials, School of Materials Science and Technology, China University of Geosciences (Beijing) 100083, China

[b] State Key Laboratory of Advanced Metallurgy, School of Metallurgical and Ecological Engineering, University of Science and Technology Beijing, Beijing, 100083, China

[c] Qinghai Provincial Key Laboratory of New Light Alloys, Qinghai Provincial Engineering Research Center of High Performance Light Metal Alloys and Forming, Qinghai University, Xining, 810016, China

* Corresponding Authors E-mail: minx@cugb.edu.cn

1. Experimental

1.1 Synthesized SnO_2 hollow spheres

$K_2SnO_3 \cdot 3H_2O$ (1.5 mmol, 0.484 g, AR) and $(NH_2)_2CO$ (8 mmol, 0.48 g, AR) were dissolved in deionized water, and the solution was stirred with a magnetic stirrer until complete dissolution. Anhydrous ethanol was then added to the solution in a 5:3 (water: ethanol) ratio, yielding a colorless, transparent solution. After stirring for approximately 30 min, a white turbid solution was formed. This solution was transferred to a PTFE liner, placed in a reactor, and heated in an electric blast drying oven at 190°C for 24 h. After the reaction, the system was allowed to cool naturally to room temperature. The reaction products were washed by centrifugation three times using water and ethanol, respectively. The washed product was then dried in a vacuum drying oven at 60°C for 8 h. The final SnO_2 hollow sphere powder was obtained.

1.2 Synthesis of SnO_2@CF

1.2 g (12%) of PAN was dissolved in 8.2 g of DMAC and stirred magnetically at room temperature for 8 hours. After complete dissolution, 0.6 g of hollow spheres of SnO_2 powder was added, and the mixture was stirred magnetically for 24h. A homogeneous SnO_2@PAN blend was obtained as the spinning solution. The solution was loaded into a 5 mL syringe equipped with a 23-gauge metal conductive needle. The SnO_2@PAN nanofiber precursor was collected by placing a nonwoven fabric receiver beneath the needle. Adjust the distance between the metal needle and the collector so that the distance between the two is 17-25 cm. The voltage setting is 15 kV positive and 2 kV negative. The syringe advancement rate was set to 0.8 mL h^{-1}. SnO_2@PAN nanofiber precursor was obtained after 5h of electrospinning. The obtained SnO_2@PAN nanofiber precursor was then pre-oxidized in a muffle furnace, with the temperature increased at a rate of 1°C min^{-1}: first to 180°C (held for 1h), then to 200°C (held for 1h), 230°C (held for 1h), and 250°C (held for 1h), followed by a final reduction to 180°C (held for 1h). Finally, the precursor was heated in a nitrogen atmosphere at 2°C min^{-1} to 500°C and held for 2h. The resulting material was carbonized SnO_2@CF.

1.3 Materials characterizations

Crystallographic structure of the samples is determined using X-ray diffractometer (XRD, Bruker D8 advanced) with CuKα radiation in the 2θ range from 10 to 90°. The Raman spectrometer (Horiba LabRAM HR Evolution) was employed to analyze the material and identify the type of carbon. Transmission electron microscopy (TEM, JEM-F200) and field emission scanning electron microscopy (FESEM, ZEISS SUPRA-55) were employed to examine the morphology and microstructure of the materials for further analysis. Energy dispersive spectroscopy (EDS, QUANTAX) analysis was conducted to obtain elemental mappings. Energy dispersive X-ray spectroscopy (EDS) and high-resolution TEM (HRTEM, JEM-F200) were employed to observe the crystal lattice spacing. X-ray photoelectron spectroscopy (XPS) was performed using a Thermo Scientific K-Alpha spectrometer, with data processed using the "Avantage.exe" software.

1.4 Electrochemical measurement

The electrochemical properties of the electrode materials were evaluated by assembling a CR2032 button battery. The active material, Super-P and PVDF were weighed in the ratio of 7:2:1. they were then placed in a mortar for initial grinding to ensure that the components were initially mixed homogeneously. Next, 400 μL of NMP was added, followed by continued grinding for 20 min to obtain a homogeneous electrode slurry. The above slurry was uniformly coated onto the copper foil using a flatbed heated coater, wherein the thickness of the squeegee was set to 10 μm. After drying in a vacuum oven for 12 h at 60° C., the coated copper foils were cut into 10 mm electrode sheets. The active substance loading of each copper foil was about ~1.9 mg cm-2. The assembly of the CR2032 half-battery was carried out in a glove box filled with argon atmosphere. The electrolyte used was 0.8 M $LiPF_6$ in DEC:EC=1:1 Vol%. The counter electrode was a lithium metal sheet with a radius of 16 mm. The assembly is then sealed using a battery packaging machine. The encapsulated batteries were left to stand for 8h and then electrochemical tests were carried out. Cycling performance

tests were performed on a CT 4008-5VmA-164 (Shenzhen Xinwei Electronics) with a voltage range of 0.01- 3.0 V. Cyclic voltammetry (CV) curves were obtained from an electrochemical workstation (CHI 660 E). Electrochemical impedance spectroscopy (EIS) was performed on an electrochemical workstation (CHI 660 E) in the frequency range of 100 kHz to 0.01 Hz. The EIS data processing software was “ZView2.exe”.

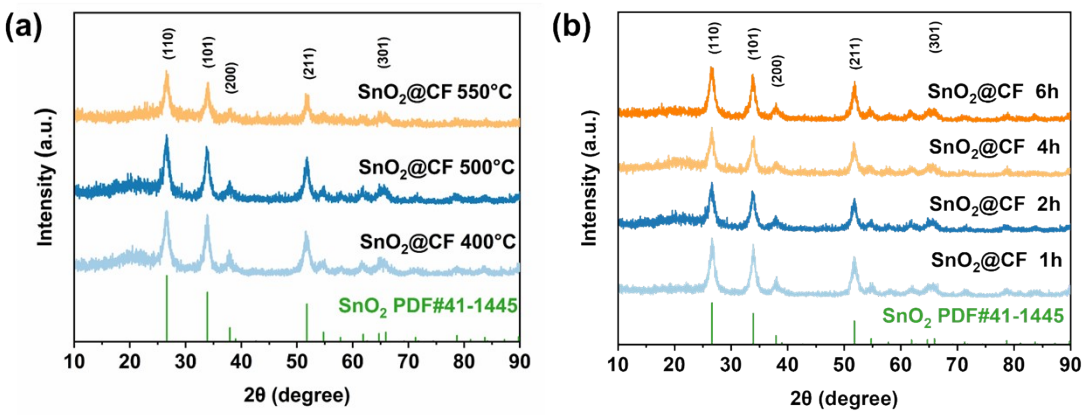

Figure S1 SnO_2@CF prepared at different heat treatment (a) temperatures and (b) times.

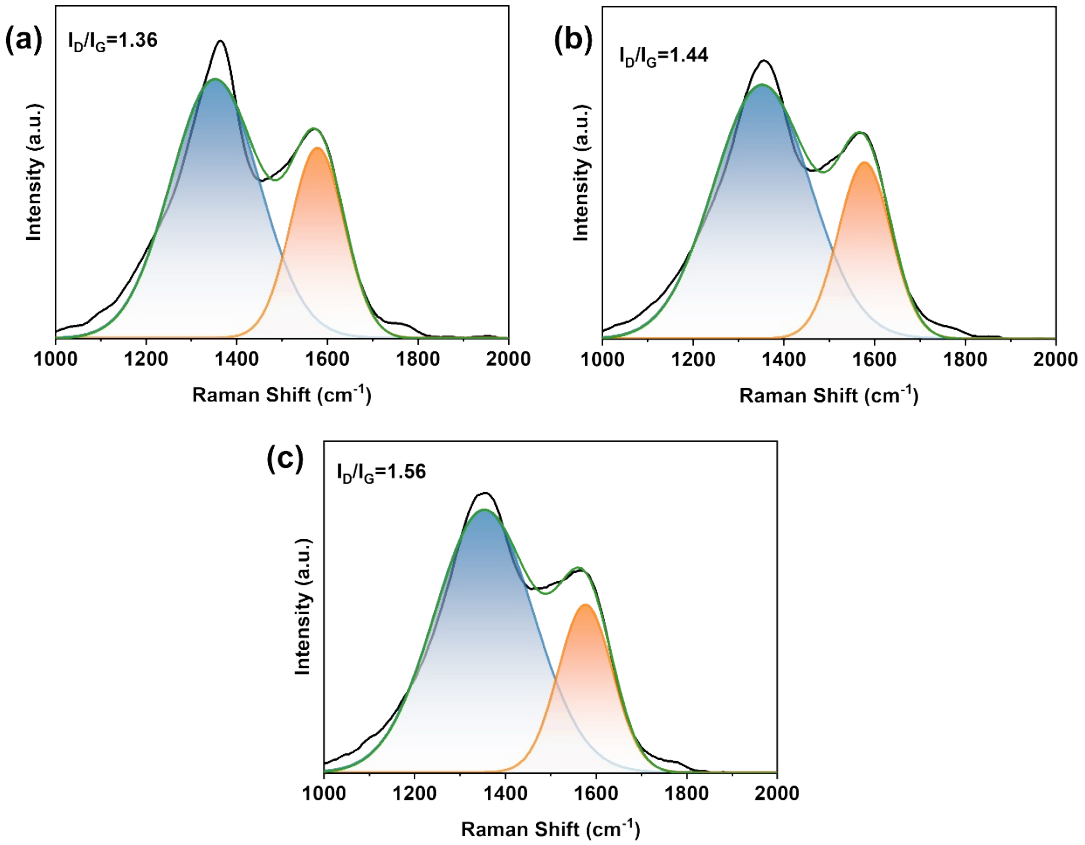

Figure S2 The intensity ratio of I_D/I_G was obtained by peak-fitting.

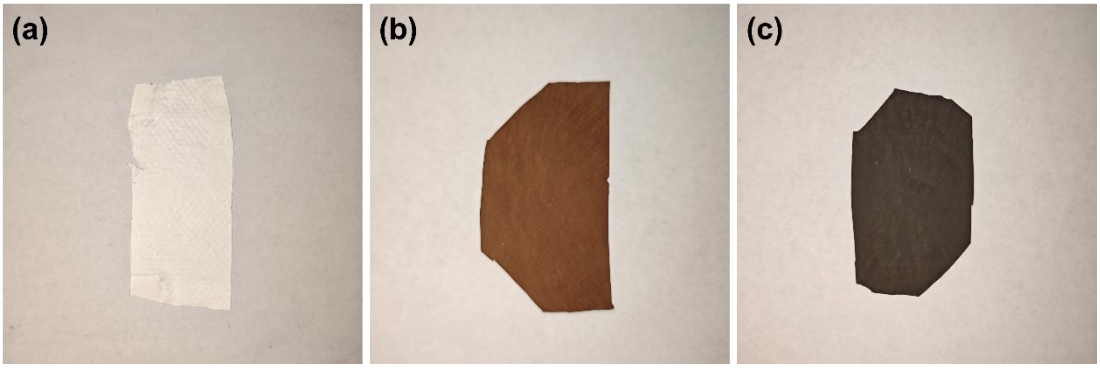

Figure S3 The digital photos: (a) The SnO_2@CF precursors. (b) The pre-oxidized product. (c) The SnO_2@CF.

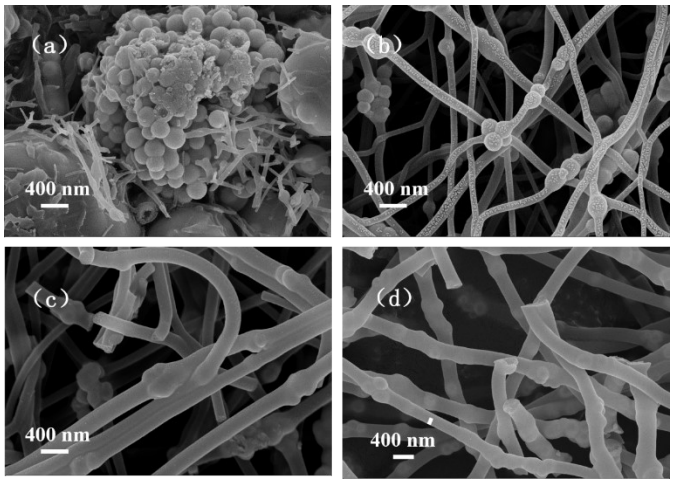

Figure S4 The SEM images of SnO_2@CF with different PAN additions: (a) PAN-8%, (b) PAN-10%, (c) PAN-12%, (d) PAN-14%.

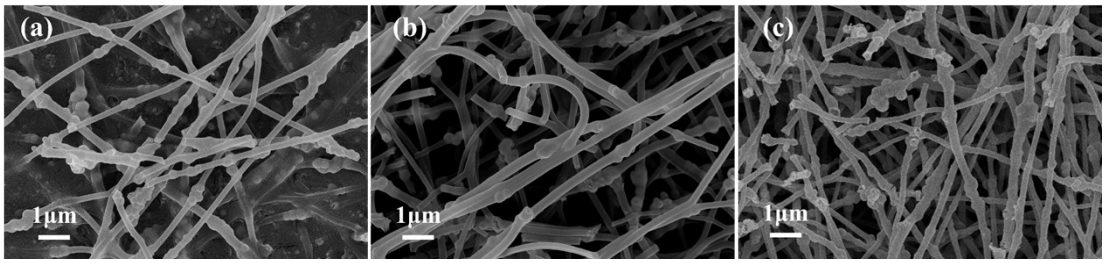

Figure S5 The SEM images of SnO_2@CF at different heat treatment temperatures: (a) 400°C, (b) 500°C, (c) 550°C.

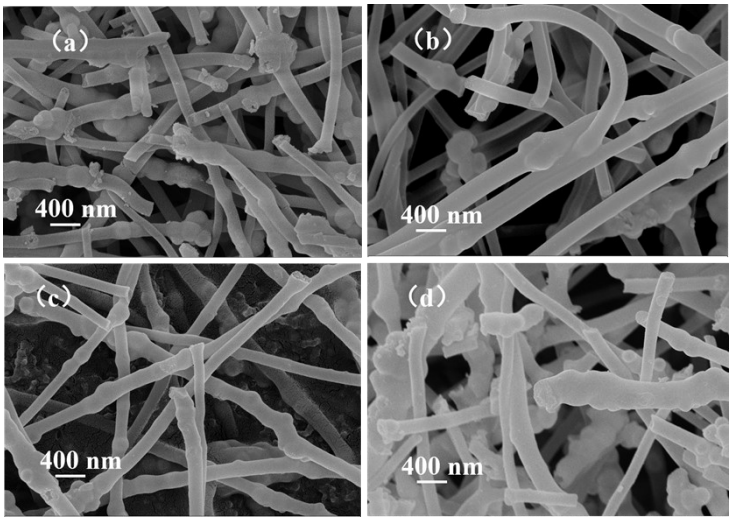

Figure S6 SEM images of SnO_2@CF with different heat treatment times: (a) 1h, (b) 2h, (c) 4h, (d) 6h.

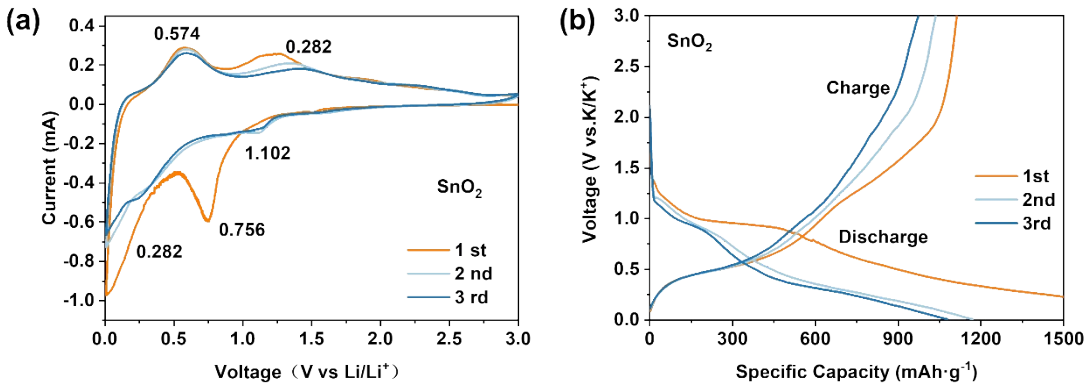

Figure S7 (a) CV curve of SnO_2 at a scan rate of 0.2 mV s^{-1}. (b)The constant current discharge/charge curves of SnO_2 at 0.2C.

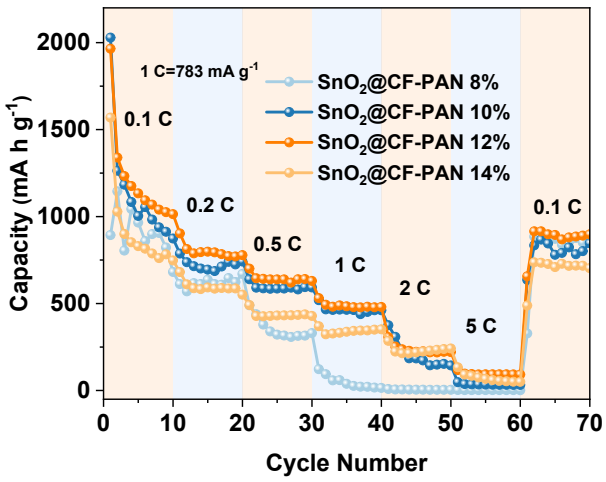

Figure S8 Rate capability of SnO_2@CF with different PAN additions.

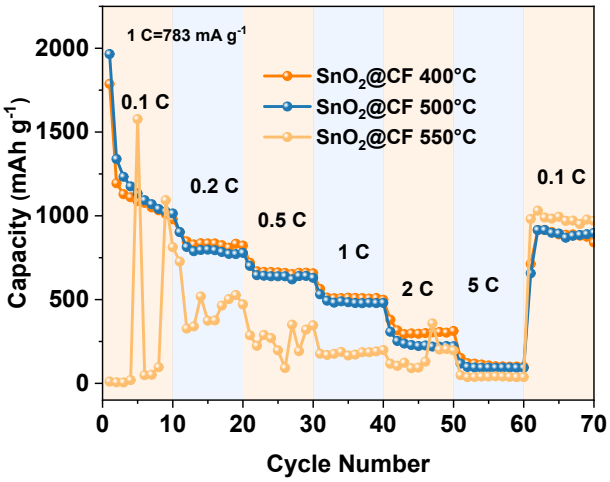

Figure S9 Rate capability of SnO_2@CF with different heat treatment temperatures.

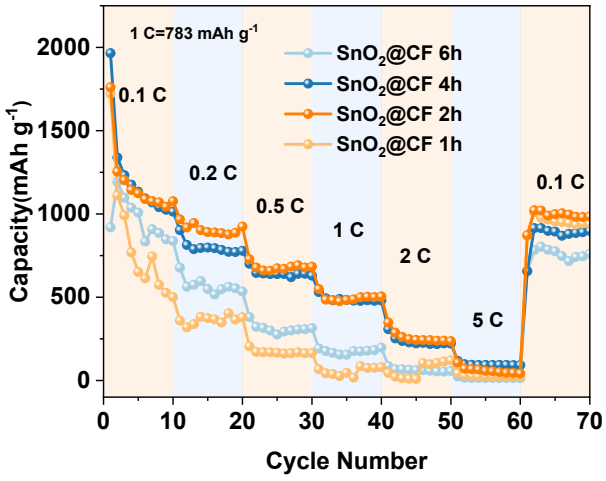

Figure S10 Rate capability of SnO_2@CF with different heat treatment times.

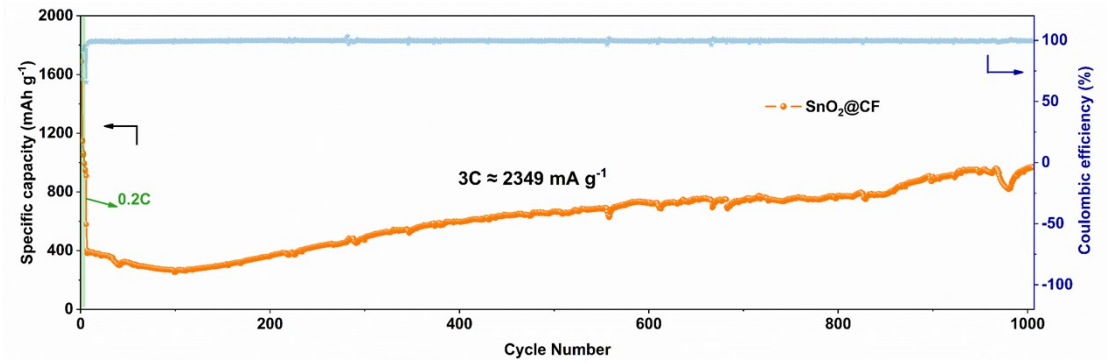

Figure S11 Long-term cycling stability of SnO_2@CF at 3C.

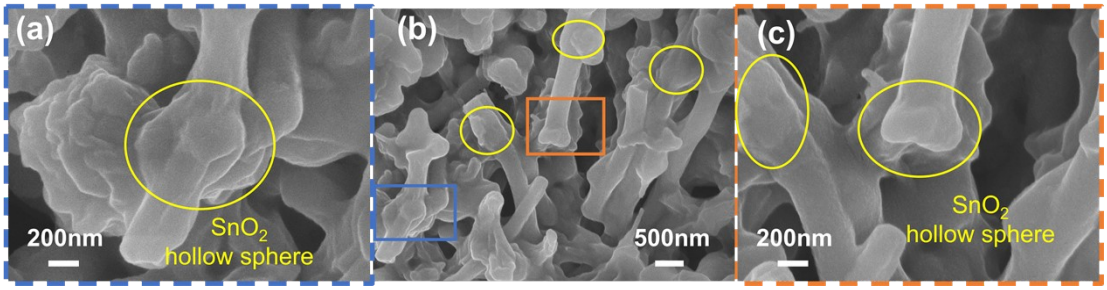

Figure S12 The post-mortem SEM images of SnO_2@CF after 250 cycles at 0.2C.

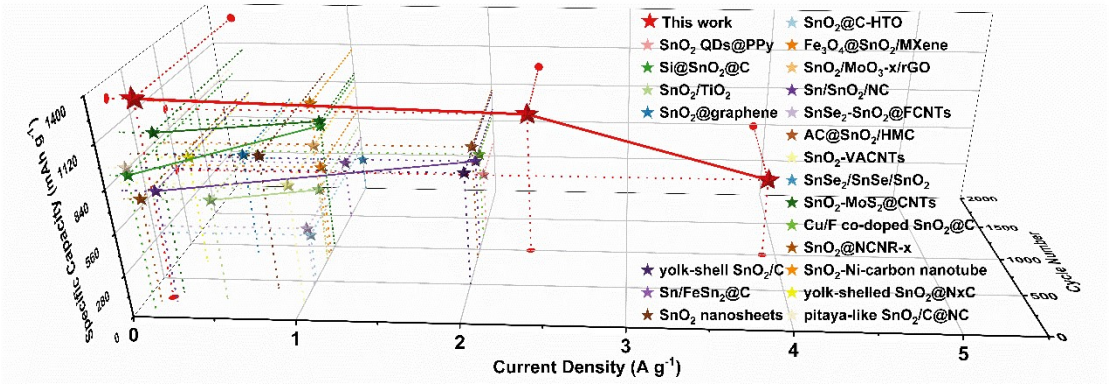

Figure S13 (f) Comparison of the cycling performance of SnO_2-based electrodes and the designed SnO_2@CF electrode.

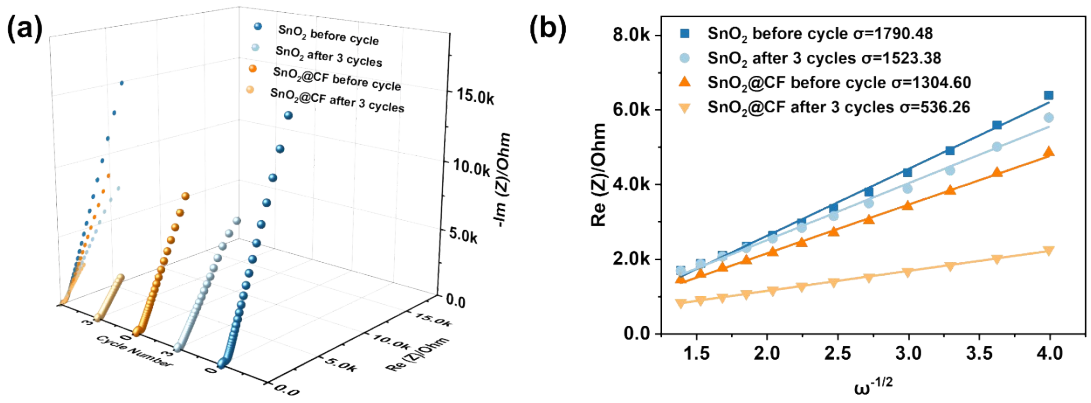

Figure S14 (a) Nyquist plots of the SnO_2@CF and SnO_2 with before and after cycling tests. (b) The fitting results of σ value.

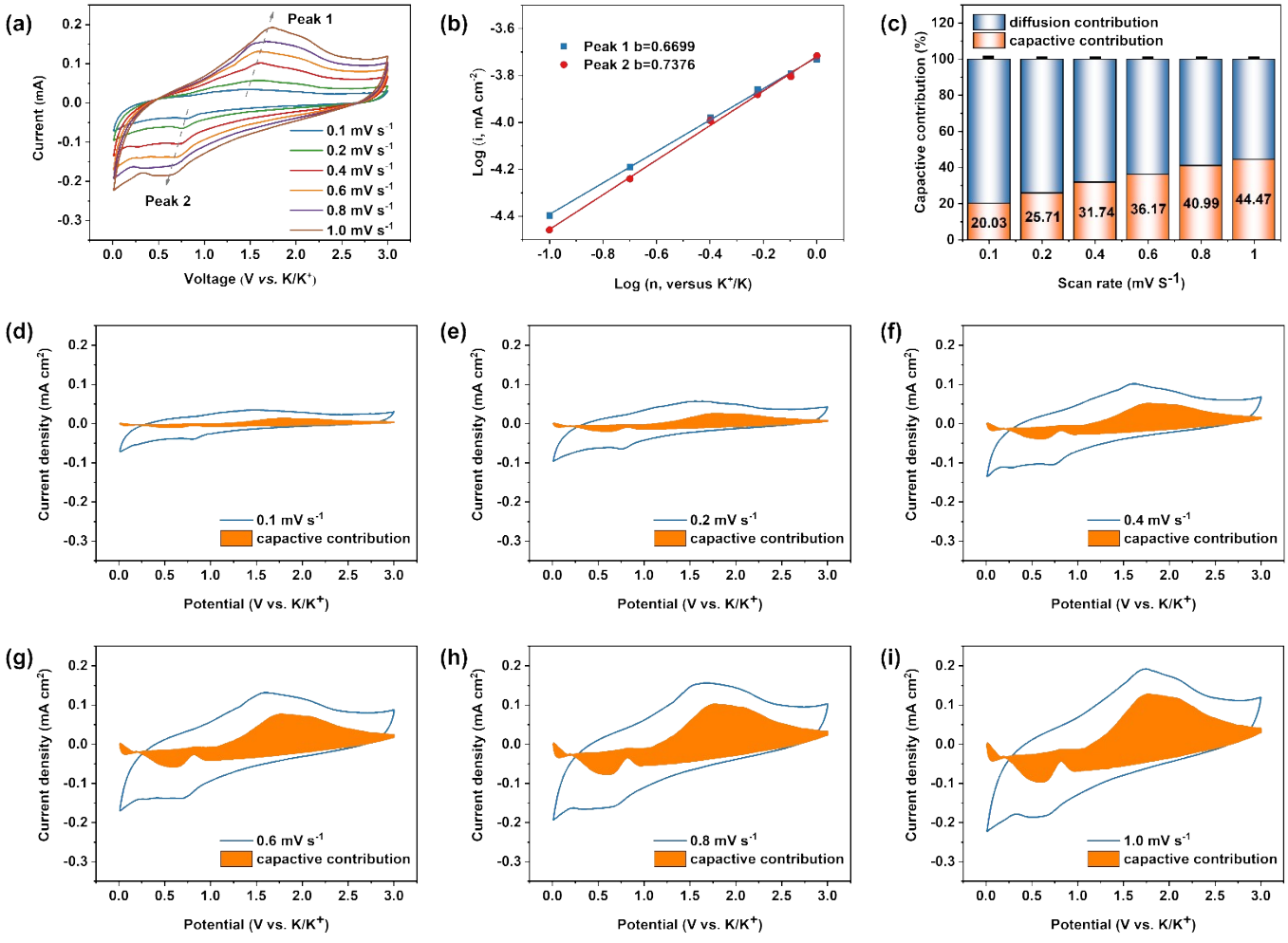

Figure S15 (a) CV curves of SnO_2@CF at gradually increasing scan rates. (b) the *b*-value of the linear regression. (c) The percentages of capacitive/diffusion contribution.

The capacitive contributions at different scan rates: (d) 0.1 mV s^{-1}, (e) 0.2 mV s^{-1}, (f) 0.4 mV s^{-1}, (g) 0.6 mV s^{-1}, (h) 0.8 mV s^{-1}, and (i) 1.0 mV s^{-1}.

The CV curves of SnO_2@CF, measured at scan rates of 0.1, 0.2, 0.4, 0.6, 0.8, and 1.0 mV s^{-1}, are shown in **Fig.** S15(a). The shape of all CV curves was well preserved, and the peak current increased with the scan rate, indicating a rapid electrochemical response of the electrode material to the embedding/de-embedding of Li^+. **Eq.** (S6) describes the relationship between scan rate and peak current. The logarithm is taken to obtain the **Eq.** (S7). When *b* approaches 0.5, the electrode is considered to exhibit diffusion-controlled behavior. Conversely, if *b* approaches 1.0, the electrode is considered to exhibit capacitance-controlled behavior. **Fig.** S15(b) shows the peaks observed in both the cathodic and anodic processes, corresponding to *b*-values of 0.6699 and 0.7376, respectively, demonstrate that the charge storage is attributed to the synergistic effect of capacitive-controlled and diffusion-controlled processes.

In addition, the contribution ratio of diffusion control and capacitance control can be described by **Eq.** (S8). In **Eq.** (S8), k_1v represents the non-Faradic response, while $k_2v^{0.5}$ corresponds to the Faradic response. By taking the logarithm of both sides of **Eq.** (S3) and dividing by $v^{0.5}$, **Eq.** (S9) is obtained, allowing for the quantitative evaluation of the capacitive contribution. The capacitive contribution distribution and its percentage share were evaluated for other scan rates (**Fig.** S15(c)). Additionally, the capacitive contributions at scan rates of 0.1, 0.2, 0.4, 0.6, 0.8 and 1.0 mV s^{-1} were found to be 20.03%, 25.71%, 31.74%, 36.17%, 40.99%, and 44.47%, respectively (**Fig.** S15(d)-(i)). Therefore, the Li storage in SnO_2@CF is dominated by the diffusion contribution.

Equation:

$$SnO_2 + 4Li^+ + 4e^- \rightarrow Sn + 2Li_2O \quad \text{(S1)}$$

$$Sn + xLi^+ + xe^- \rightarrow Li_xSn\ (0 < x < 4.4) \quad \text{(S2)}$$

$$Li_xSn \rightarrow Sn + xLi^+ + xe^-\ (0 < x < 4.4) \quad \text{(S3)}$$

$$Sn/SnO + LiO_2 \rightarrow SnO/SnO_2 + 2Li^+ + 2e^- \quad \text{(S4)}$$

$$Z_{real} = R_e + R_{ct} + \sigma\omega^{1/2} \quad \text{(S5)}$$

$$i = av^b\ (0.5 < b < 1.0) \quad \text{(S6)}$$

$$log(i) = b\ log(v) + log(a) \quad \text{(S7)}$$

$$i = k_1v + k_2v^{0.5} \quad \text{(S8)}$$

$$i / v^{0.5} = k_1v^{0.5} + k_2 \quad \text{(S9)}$$

Table S1 Comparison results of cycling performances between the SnO_2@CF and other recently reported SnO_2-based anode materials for LIBs.

Electrodes	Current density (A g^{-1})	Cycle number	Specific capacity (mA h g^{-1})	Ref.
SnO_2@CF	**0.16 (0.2C)**	**250**	**1301**	**This work**
	2.3 (3C)	**1000**	**973**	
	3.9 (5C)	**1000**	**548**	
SnO_2 QDs@PPy	2.0	1360	399	1
Si@SnO_2@C	1.0	1000	874.3	2
	0.1	100	888.7	
SnO_2/TiO_2	0.5	250	673.7	3
	1.0	800	510.5	
SnO_2@graphene	0.5	900	703.1	4
SnO_2@C-HTO	1.0	500	330	5
Fe_3O_4@SnO_2/MXene	1.0	900	626.1	6
SnO_2/MoO_{3-x}/rGO	1.0	800	813	7
Sn/SnO_2/NC	0.2	200	747.9	8
	2.0	1000	644.1	
$SnSe_2$-SnO_2@FCNTs	1.0	450	400	9
AC@SnO_2/HMC	2.0	800	792.1	10
SnO_2-VACNTs	1.0	200	800	11
$SnSe_2$/SnSe/SnO_2	1.0	2000	233	12
SnO_2-MoS_2@CNTs	0.2	320	1069.3	13
	1.0	1000	904.5	
Cu/F co-doped SnO_2@C	2.0	1200	612	14
SnO_2@NCNR-x	0.1	200	694.2	15
SnO2–Ni-carbon nanotube	1.0	850	1078.2	16
yolk-shell SnO_2/C	2.0	500	771	17
Sn/$FeSn_2$@C	1.0	1500	409	18
SnO_2 nanosheets	0.782	400	901.2	19
yolk-shelled SnO_2@NxC	0.2	750	740	20
pitaya-like SnO_2/C@NC	0.1	100	936.8	21

Reference

1. K. S. Rao, D. D. Pathak, B. P. Mandal, S. Samanta and A. K. Tyagi, *Acs Appl Electron Ma*, 2024, **6**, 3454-3463.
2. C. X. Sun, J. H. Pan, X. M. Fu, D. C. Ma, L. Y. Cui, W. K. Yao, C. X. Jiao, Y. P. Xu, H. X. Hao, M. Li, A. Du and Q. Wang, *Mater Today Sustain*, 2024, **27**.
3. Q. J. Ge, Z. H. Ma, M. L. Yao, H. Dong, X. Y. Chen, S. Q. Chen, T. H. Yao, X. Ji, L. Li and H. K. Wang, *Journal of Colloid and Interface Science*, 2024, **661**, 888-896.
4. H. Li, Y. Zhuang, H. Y. Qi, C. B. Zheng, Z. T. Wang, H. Yao, Z. Q. Liu, Y. Y. Li, J. Q. He, W. K. Zou, J. Zhu and S. Y. Yin, *Energy Technol-Ger*, 2024, **12**.
5. Z. H. Chen, T. Wang, Y. Liu, Y. C. Liu and X. P. Yang, *Chemical Engineering Journal*, 2024, **483**.
6. X. Duan, J. Q. Liu, F. S. Lv, T. Liu, W. B. Cui, J. Wang, Q. Wang and S. Yuan, *Journal of Energy Storage*, 2024, **86**.
7. J. H. Li, L. Wei, X. K. Cui, G. X. Han, S. Y. Hou, W. C. Shen, F. Y. Kang, R. T. Lv, L. Q. Ma and Z. H. Huang, *Electrochimica Acta*, 2024, **503**.
8. Z. Z. Shen, X. T. Guo, H. Y. Ding, D. H. Yu, Y. H. Chen, N. N. Li, H. J. Zhou, S. T. Zhang, J. Wu and H. Pang, *Nano Res*, 2024, **17**, 9721-9727.
9. W. J. Yu, B. C. Deng, T. H. An, J. Wang, Y. Ji, G. Q. Mao, H. Y. Cai, H. Zhang, H. Tong, H. B. He and C. P. Liang, *J Alloy Compd*, 2025, **1010**.
10. X. B. Wang, K. X. Huo, Z. Q. He, J. L. Liu, Q. S. Zhao, J. Q. Zhang and M. B. Wu, *J Power Sources*, 2024, **615**.
11. A. Thapa, A. R. Baboukani, P. Siwakoti, K. L. Jungjohann, C. E. Nwanno, J. D. Zhang, C. L. Wang, H. W. Gao and W. Z. Li, *J Power Sources*, 2025, **625**.
12. J. M. Liu, T. Zhou, Y. Shen, P. Zuo, H. Qiu, Y. J. Zhu and J. Y. Liu, *Chem Commun*, 2024, **60**, 13079-13082.
13. C. K. Jiang, W. B. Ye, H. T. Xu, Z. Y. Feng, D. P. Xiong and M. He, *Acs Appl Mater Inter*, 2024, **16**, 44900-44911.
14. S. X. Huang, L. J. Guo, W. Liu, C. J. Hang, R. An, Y. F. Li and Y. H. Tian, *Chemical Engineering Journal*, 2024, **496**.
15. H. Q. Yang, B. Wang, Y. D. Li, H. M. Du, J. S. Zhao and Y. Xie, *J Alloy Compd*, 2023, **945**.
16. W. B. Ye, Z. Y. Feng, D. P. Xiong and M. He, *Acs Appl Nano Mater*, 2023, **6**, 16524-16535.
17. X. T. Jia, H. Y. Li, B. Huang, J. W. Yang and Y. W. Li, *Adv Powder Technol*, 2023, **34**.
18. M. Chen, P. Xiao, K. Yang, B. X. Dong, D. Xu, C. Y. Yan, X. J. Liu, J. T. Zai, C. J. Low and X. F. Qian, *Angew Chem Int Edit*, 2023, **62**.
19. Z. Q. Hu, M. Y. Wang, H. M. Yang, C. Liang and K. F. Yu, *Diam Relat Mater*, 2022, **126**.
20. B. Li, Y. F. Song, Y. X. Wang, Z. He and W. Gao, *Mater Design*, 2022, **219**.
21. X. Liu, S. Zhang, P. Zhang, Z. M. Zheng, F. Bai and Q. Li, *Nanoscale*, 2023, **15**, 1669-1675.